scientific reports

Check for updates

OPEN

Ultra-large nonlinear parameters and all-optical modulation of a transition metal dichalcogenides on silicon waveguide

Tianyang Ding✉, Siqin Xu & Xianlong Sun

We integrate monolayer TMDCs into silicon-on-insulation (SOI) waveguides and dielectric-loaded surface plasmon polariton (DLSPP) waveguides to enhance nonlinear parameters (γ) of silicon-based waveguides. By optimizing the waveguide geometry, we have achieved significantly improved γ. In $MoSe_2$-on-SOI and $MoSe_2$-in-DLSPP waveguide with optimized geometry, the maximum γ at the excitonic resonant peak (λ_p) is 5001.87 $W^{-1}m^{-1}$ and 119111.94 $W^{-1}m^{-1}$ respectively for each case. Based on this, we designed all-optical TMDCs-on-SOI phase and extinction waveguide modulators, achieving π-phase and 3 dB modulation with millimeter-scale modulation lengths under an optical pump intensity of 1 GW/cm^2 at the optical communication wavelengths of 1310 nm and 1550 nm. At the λ_p of $MoSe_2$, a modulation length of only 75 μm is required for π-phase modulation, while a modulation length of 1.36 mm is sufficient for 3 dB modulation. Our work provides new insights for achieving miniaturized and low-power optical communication and networking applications.

Silicon-based electronic microprocessors have experienced a flourishing period of 40 years. However, with the rapid advancement in advanced engineering computing, data analytics, and cloud computing, silicon-based electronic processors are no longer capable of meeting the escalating demand for ultra-fast and energy-efficient computation[1]. In this regard, silicon photonics emerges as an appealing solution due to its low cost and excellent compatibility with mature CMOS industry. Modulation in all-optical computing for silicon photonics is achieved through nonlinear phenomena. Nevertheless, it should be noted that silicon possesses a relatively low Kerr coefficient (n_2)[2]. Consequently, achieving a satisfactory optical modulation effect requires excessively high light intensity and necessitates lengthy device lengths. To overcome these limitations effectively, integration of novel materials exhibiting exceptional nonlinear-optical coefficients into silicon photonic platforms has been identified as an ideal approach[3–6]. For instance, waveguides integrated with graphene have achieved high nonlinear parameters[7], high-performance vertical van der Waals heterostructure-based photodetectors are successfully integrated on a silicon photonics platform[8], and silicon nitride-on-silicon waveguide photodetectors integrated in a visible light photonic platform on silicon have attained a high external quantum efficiency[9].

Two-dimensional transition metal dichalcogenides (TMDCs) are a highly promising class of two-dimensional nanomaterials. The chemical composition of TMDCs can be expressed as MX_2 (M = Mo, W, etc.; X = S, Se, etc.), with the M layer sandwiched between two X layers[10]. Due to their unique two-dimensional confinement of electron motion and absence of interlayer perturbation, TMDCs have found extensive applications in photodetectors[11], photocatalysis[12], and mode lockers[13]. Theoretical calculations and experimental measurements have revealed that monolayer TMDCs exhibit significant binding energy (0.5 - 1 eV) for their two-dimensional excitons[14]. This large binding energy enables a series of exciton levels to serve as final or even intermediate states for optical parametric amplification (OPA) or two-photon absorption (2PA)[15,16]. Notably, studies have demonstrated that TMDCs possess substantial nonlinear coefficients in certain near-infrared regions. In comparison with zero-bandgap graphene, the considerable bandgaps of monolayer TMDCs prevent them from significant linear absorption loss at infrared telecommunication wavelengths[3,17]. It is anticipated that by integrating TMDCs into silicon waveguides instead of graphene, one can mitigate the high optical losses associated with graphene while harnessing the remarkable n_2 offered by TMDCs.

In this paper, we integrate monolayer TMDCs into silicon-on-insulator (SOI) waveguides and dielectric-loaded surface plasmon polariton (DLSPP) waveguides. We exploit the excitonic resonant enhanced β and n_2 of monolayer TMDCs to enhance the nonlinear parameter (γ) of silicon waveguides. By optimizing the geometry

MOE Key Laboratory of Laser Life Science, Institute of Laser Life Science, College of Biophotonics, South China Normal University, Guangzhou 510631, China. ✉email: 2021023336@m.scnu.edu.cn

of the TMDCs-based waveguide, we achieve a substantial enhancement in γ of the waveguide at the excitonic resonant peak (λ_p = 1172 nm) and telecommunications wavelength of 1310 nm, 1550 nm. Subsequently, we conduct further investigation on the γ maxima of TMDCs-based waveguides within the wavelength range from 1100 to 1550 nm, employing optimized waveguide geometry. Further, the giant γ and long-range waveguiding properties of the acquired integrated waveguides with optimized structures are used as both extinction and phase modulators to demonstrate superb all-optical switching performance. Finally, we present the phase and extinction modulation performance of TMDCs-on-SOI waveguides in optimized structures. Significantly, this study may enable novel ways for next-generation nonlinear all-optical modulation applications.

Results and discussion

Characterization of monolayer TMDCs

In monolayer TMDCs, the refractive index of the material offers the most fundamental description of light-matter interaction. Ellipsometry has been proven to be an effective non-destructive method for characterizing the optical properties of monolayer TMDCs, offering crucial insights into film refractive index, extinction coefficient, and thickness[18]. In recent years, a large number of studies have employed ellipsometry to measure the complex refractive index of TMDCs[19–21]. The theoretical treatment of TMDCs' optical properties is complex, notably due to spin-orbit coupling and strong excitonic effects resulting from electron-hole interactions[22,23]. Therefore, in the simulations conducted in this study, we directly utilize the experimental values of monolayer TMDCs refractive index obtained at room temperature, as reported in the Ref.[24].

Within monolayer TMDCs, there exist two characteristic excitonic states known as exciton A and exciton B. Recently, Ji et al. conducted a systematic theoretical study based on quantum perturbation theory, revealing that the strong excitonic resonant effects in highly-crystalline monolayer TMDCs lead to significantly enhanced β[15,16]. Based on second-order, time-dependent quantum perturbation theory, β of monolayer TMDCs can be calculated by:

$$\beta(hv) = CNhv\left[\frac{E_{loc}}{E}\right]\left[\frac{|\mu_{gg}|^2}{(E_A - hv)^2 + (\Gamma_A/2)^2} + \frac{|\mu_{gg}|^2}{(E_B - hv)^2 + (\Gamma_B/2)^2}\right] \times \left[\frac{|\mu_{fg}|^2\,\Gamma_f/2\pi}{(E_{fg} - 2hv)^2 + (\Gamma_f/2)^2}\right] \quad (1)$$

where hν is the photon energy, N represents the density of active unit cells, E_{loc}/E refers to the local-field correction factor, E_i and Γ_i correspond to transition energy of a certain energy level and its linewidth, respectively, μ_{ij} denotes the transition dipole moment, C is a material-independent constant. By substituting eq.1 into Kramers-Krönig transformation, we can obtain n_2 of the monolayer TMDCs. it is assumed that only the 2p excited states are involved in the 2PA process, while other excitonic states are completely ignored[25]. The spectra of n_2 and β are shown in Fig. 1.

Giant nonlinear parameters of the monolayer-TMDCs-silicon waveguides

As shown in Fig. 2, Two typical photonic and plasmonic silicon-waveguide structures have been made use of to optimize electric-field interaction with monolayer TMDCs and maximize the γ. Firstly, the representative SOI waveguide is employed, which is a photonic waveguide and composed of SiO_2 substrate beneath a silicon slab with air as the overcladding. Monolayer TMDCs are deposited on top of the silicon slab and cover the prime mode-area of the silicon slab. Both the fundamental quasi-TM and quasi-TE modes are considered. Secondly, to concentrate optical modes intensity on the top surface of the SOI waveguide and achieve greater interaction between monolayer TMDCs and fundamental optical modes, a DLSPP waveguide is employed. In the DLSPP waveguide integrated with monolayer TMDCs, 50 nm of gold is added on top of the first waveguide configuration

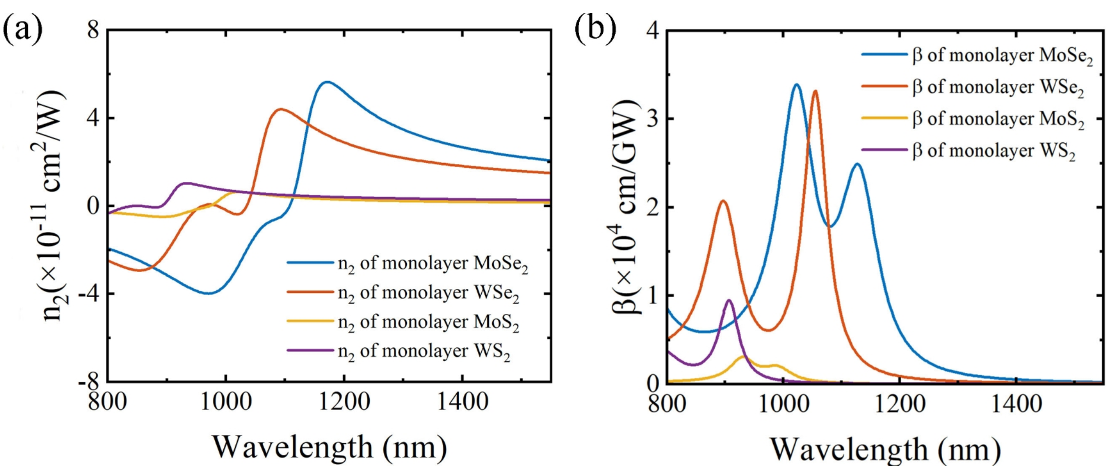

Fig. 1. (**a**) Kerr coefficients n_2 of the monolayer TMDCs in 800 - 1550 nm. (**b**) Two-photon absorption coefficients β of the monolayer TMDCs in 800 - 1550 nm.

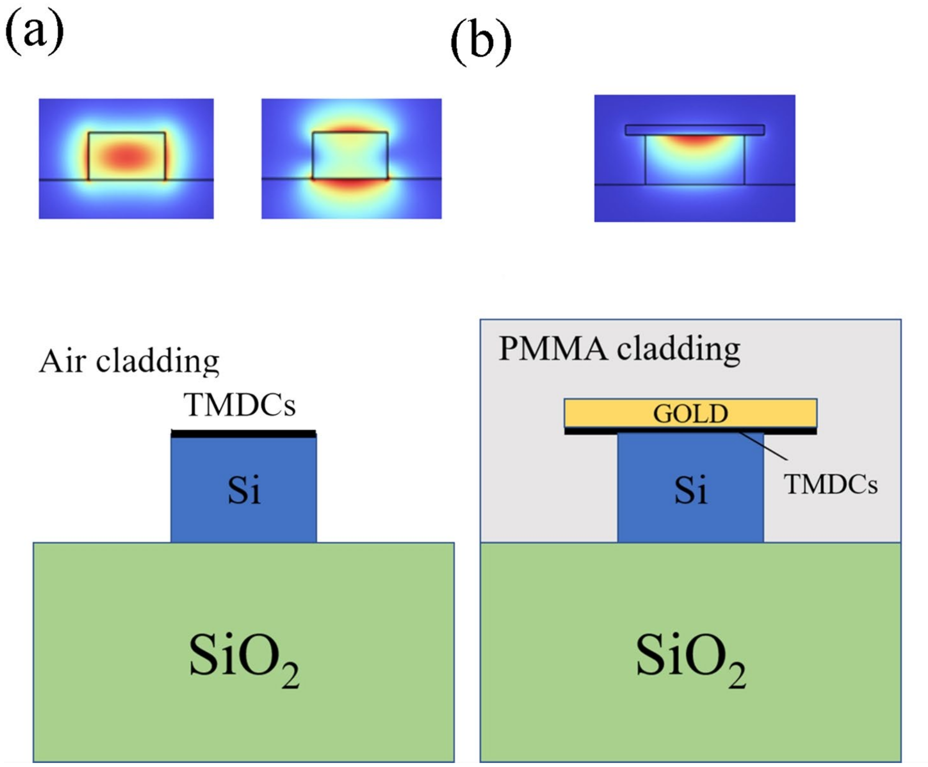

Fig. 2. (**a**) Schematic diagram of silicon channel waveguide with monolayer TMDCs (the upper inset shows the electric-field distribution $|E|$ in quasi-TE and quasi-TM modes for a silicon channel waveguide). (**b**) Schematic diagram of DLSPP waveguide consisting of a silicon core, monolayer of TMDCs, PMMA cladding, and a 50 nm Au layer (the upper inset shows the electric-field distribution $|E|$ in TM mode for a DLSPP waveguide).

and the overcladding is replaced by PMMA, whose refractive index is close to that of SiO_2. Only TM-like surface plasmon polaritons parallel to the boundary between gold and Si are supported in the DLSPP waveguide.

The effective third-order nonlinearity of the integrated waveguides is characterized by their γ, which takes account of both the transverse dependence of the nonlinear coefficients and the effective optical mode area (A_{eff}) of the waveguide. Taking consideration of the large refractive index contrast in the integrated waveguides, γ could be quantitatively evaluated by[26]:

$$Re\left(\gamma\right)=\frac{2\pi}{\lambda}\frac{\iint_D n_0^2\left(x,y\right)n_2\left(x,y\right)S_z^2dxdy}{\left[\iint_D n_0\left(x,y\right)S_z\left(x,y\right)dxdy\right]^2} \tag{2}$$

$$Im\left(\gamma\right)=\frac{2\pi}{\lambda}\frac{\iint_D n_0^2\left(x,y\right)k_2\left(x,y\right)S_z^2dxdy}{\left[\iint_D n_0\left(x,y\right)S_z\left(x,y\right)dxdy\right]^2} \tag{3}$$

where S_z is time-averaged Poynting vector, D refers to the integral of the electric-field over the material regions, n_0 corresponds to linear refractive index of material, n_2 denotes the Kerr coefficients of material, k_2 is nonlinear extinction coefficients. The definition of γ highlights the importance of waveguide design in achieving optimal electric-field interaction with monolayer TMDCs. We carry out the calculations over a broad wavelength range from the first λ_p wavelength to the telecommunication wavelength of 1550 nm. In the subsequent calculations, the values of n_2 and β for silicon are obtained from Ref.[2]. Additionally, the values of n_0 and k_0 for silicon, SiO_2, PMMA are obtained from the experimentally determined results in Refs.[26–28], respectively.

Firstly, we investigate the optimization of geometry for the monolayer-TMDCs-on-SOI waveguides so as to attain the optimal Re(γ) and Im(γ), as demonstrated in Fig. 3. Taking monolayer-$MoSe_2$-on-SOI waveguides as an example, Fig. 3a–f demonstrate the dependence of Re(γ) and Im(γ) for the fundamental quasi-TE mode on the geometry at three representative wavelengths (λ_p = 1172 nm and telecommunication wavelength λ = 1310 nm, 1550 nm), respectively. At 1172 nm, the waveguide geometry is optimized to be 440 × 70 nm to achieve the maximized absolute values of Re(γ) and Im(γ) reaching up to 5.00×10^3 and 8.91×10^3 $W^{-1}m^{-1}$. In addition, under the excitation at 1310 nm, the largest absolute values of Re(γ) and Im(γ) up to 1.98×10^3 $W^{-1}m^{-1}$ and 7.25×10^2 $W^{-1}m^{-1}$ have been attained at the optimal waveguide geometry of 490 × 80 nm. Furthermore, the

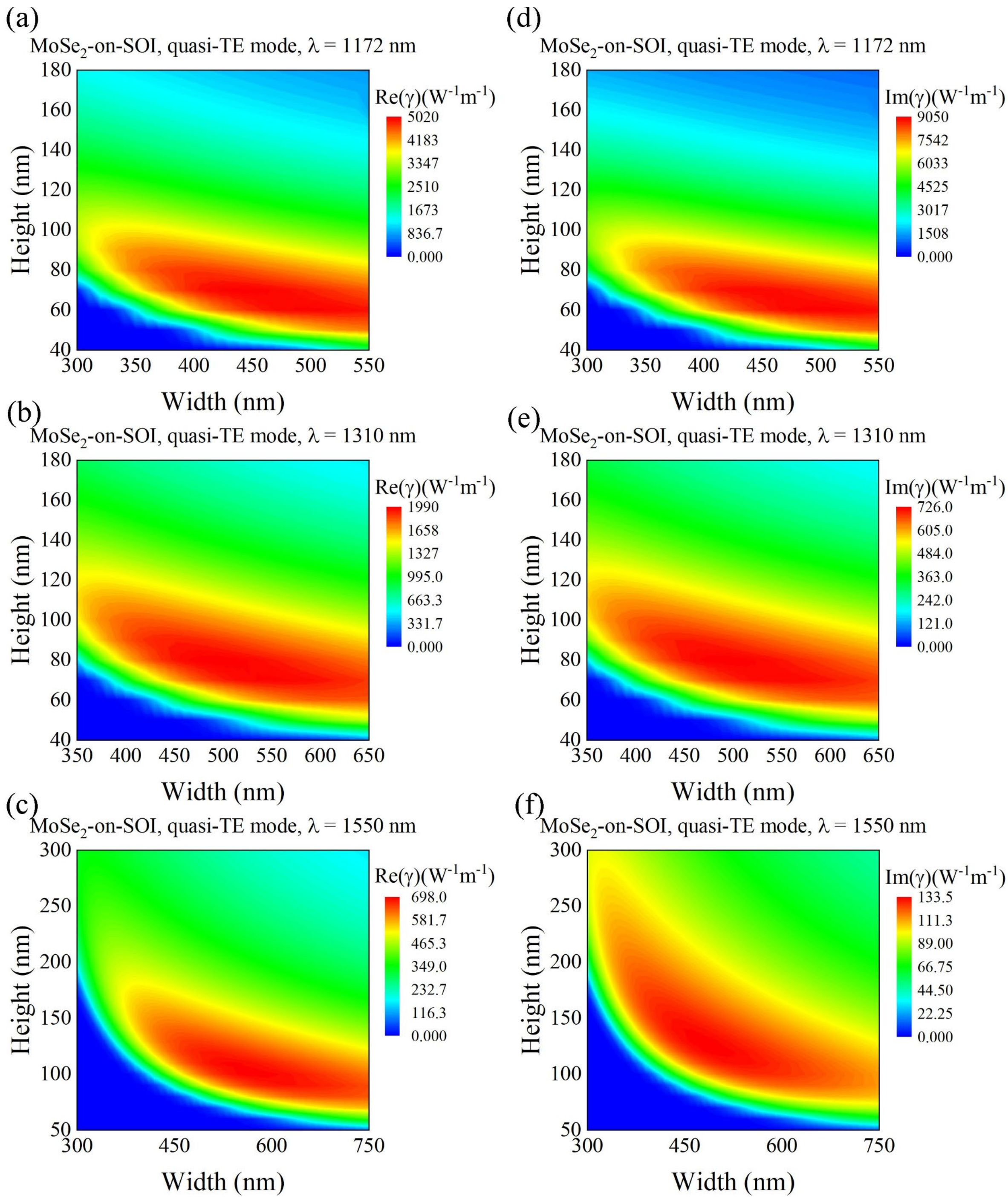

Fig. 3. Real part of nonlinear parameters of monolayer-$MoSe_2$-on-SOI waveguide in quasi-TE mode as a function of waveguide core width (x-axis) and height (y-axis) at (**a**) 1172 nm, (**b**) 1310 nm, (**c**) 1550 nm, and imaginary part of nonlinear parameters at (**d**) 1172 nm, (**e**) 1310 nm, and (**f**) 1550 nm. The insets show the waveguide cross sections when the maximum nonlinear parameter is taken at the respective wavelengths, respectively.

best waveguide geometry of 580 × 100 nm and 480 × 130 nm are exploited to realize the highest absolute values of Re(γ) and Im(γ) up to 7.51×10^2 $W^{-1}m^{-1}$ and 1.13×10^2 $W^{-1}m^{-1}$ at the mostly used telecommunication wavelength of 1550 nm. Importantly, the achieved Re(γ) and Im(γ) at the three wavelengths have been significantly improved in comparison to that of pure SOI waveguides, especially in λ_p, as revealed in the Fig. 4. Simultaneously, we conduct a tolerance analysis on the monolayer-MoSe2-on-SOI waveguide optimized geometry, as shown in Table S1 (see the Supplementary Material) . On the other side, the considerable bandgaps of monolayer TMDCs can exempt our waveguides from large linear absorption loss, which is remarkable in

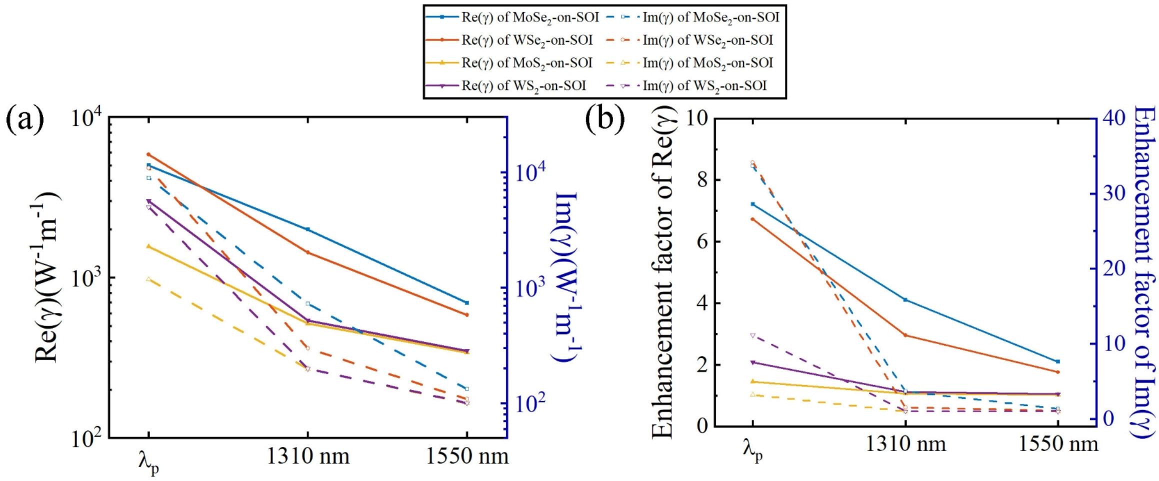

Fig. 4. (**a**) Maximum nonlinear parameters obtained at three different wavelengths exciton resonance peak λ_p = 1172 nm, communication wavelength λ = 1310 nm, 1550 nm) in the quasi-TE mode of the monolayer-$MoSe_2$-on-SOI waveguide, and (**b**) its comparison with the nonlinear parameters of the pure SOI waveguide.

graphene-silicon waveguides. In the comparison among the maximized Re(γ) and Im(γ) at the three distinct wavelengths, the greatest values attained at 1172 nm result from the enhanced n_2 together with the best electric-field overlap with monolayer $MoSe_2$ laterally and the strongest optical-mode confinement. It has been disclosed that smaller optimized waveguide geometry at shorter wavelengths lead to superior electric-field overlap with monolayer TMDCs laterally and more intense optical-mode confinement. This in combination with the larger n_2 at 1310 nm results in about 3 times greater Re(γ) than that at 1550 nm. Therefore, the interplay of three factors originating from wavelength-dependent n_2, electric-field overlap with monolayer $MoSe_2$ laterally, and optical-mode confinement gives rise to the spectral dependence of the maximized Re(γ) and Im(γ) of the $MoSe_2$-on-SOI waveguides over a broad wavelength range from 1100 to 1550 nm, as shown in Fig. S1 (see the Supplementary Material). In comparison with the quasi-TE mode, quasi-TM mode for the waveguides exhibits significantly reduced optical intensity and the resultant much weaker electric-field interaction with monolayer TMDCs. As a consequence, the nonlinear parameters for the quasi-TM mode are several times smaller than those for the quasi-TE mode, as demonstrated in Fig. S5 (see the Supplementary Material).

In order to fully understand the nonlinear optical interaction in the monolayer-TMDCs-on-SOI waveguides and optimize their performance, we further study the nonlinear parameters of monolayer MoS_2-, WS_2-, WSe_2-on-SOI waveguides. Fig. 4 also illustrates the summary and comparison of the maximum Re(γ) and Im(γ) for the essential quasi-TE mode of the monolayer MoS_2-, $MoSe_2$- WS_2-, WSe_2-on-SOI waveguides at the three representative wavelengths (λ_p, telecommunication wavelength λ = 1310 nm, 1550 nm). As a result of the superb NLO characteristics of monolayer-TMDCs, all the monolayer-TMDs-on-SOI waveguides exhibit much superior nonlinear parameters compared to that of pure SOI waveguides. Moreover, Figs. S2-S4 (see the Supplementary Material) demonstrate the spectral dependence of the maximized Re(γ) and Im(γ) of monolayer- MoS_2-, WS_2-, WSe_2-on-SOI waveguides over a wide wavelength range from 1100 to 1550 nm. Similar to the case in monolayer-$MoSe_2$-on-SOI waveguides, the quasi-TM mode for the MoS_2-, WS_2-, WSe_2-on-SOI waveguides possess substantially reduced electric-field intensity and the resultant much weaker electric-field interaction with monolayer TMDCs. Hence, the nonlinear parameters and the contribution from nonlinearity of TMDCs layers for the quasi-TM mode are much smaller than that for the quasi-TE mode, as demonstrated in Fig. S6 (see the Supplementary Material).

Secondly, we utilize the DLSPP waveguide to concentrate the electric-field intensity to the boundary between gold and silicon significantly enhancing the electric-field interaction with monolayer $MoSe_2$. This enhancement could further promote the nonlinear parameters of the waveguides. Similar to the above case, we optimize the geometry of the DLSPP waveguides to obtain the best Re(γ) and Im(γ), as shown in Fig. 5. The electric-field is intensely confined in the gold-Si interface where the monolayer $MoSe_2$ resides. The excellent overlap between monolayer $MoSe_2$ and the electric-field could lead to optimal light-matter interaction. Thanks to the strong optical confinement and the great electric-field overlap with monolayer TMDCs laterally, the resultant nonlinear parameters of monolayer-TMDCs-integrated-DLSPP waveguides are up to two orders of magnitude superior than that of the monolayer-TMDCs-on-SOI waveguides. Especially, the optimized geometry of 200 × 80 nm for the monolayer-$MoSe_2$-in-DLSPP waveguide has been employed to attain the maximized absolute values of Re(γ) and Im(γ) at 1172 nm, which reach up to 1.19×10^5 $W^{-1}m^{-1}$ and 2.25×10^5 $W^{-1}m^{-1}$. These values are more than approximately 20 and 25 times higher compared to those of the monolayer-$MoSe_2$-on-SOI waveguides, respectively. In addition, the highest absolute values of Re(γ) and Im(γ) up to 4.15×10^4 $W^{-1}m^{-1}$ and 1.48×10^4 $W^{-1}m^{-1}$ have been achieved at 1310 nm, which are approximately 20 times superior compared to that of the monolayer-$MoSe_2$-on-SOI waveguides. Moreover, at the mostly used telecommunication wavelength of 1550 nm, the realized greatest absolute values of Re(γ) and Im(γ) reach 9.97×10^3 $W^{-1}m^{-1}$ and 1.41×10^2 $W^{-1}m^{-1}$, respectively, which are 14 and 10 times larger than that of the monolayer-$MoSe_2$-on-SOI waveguides. We

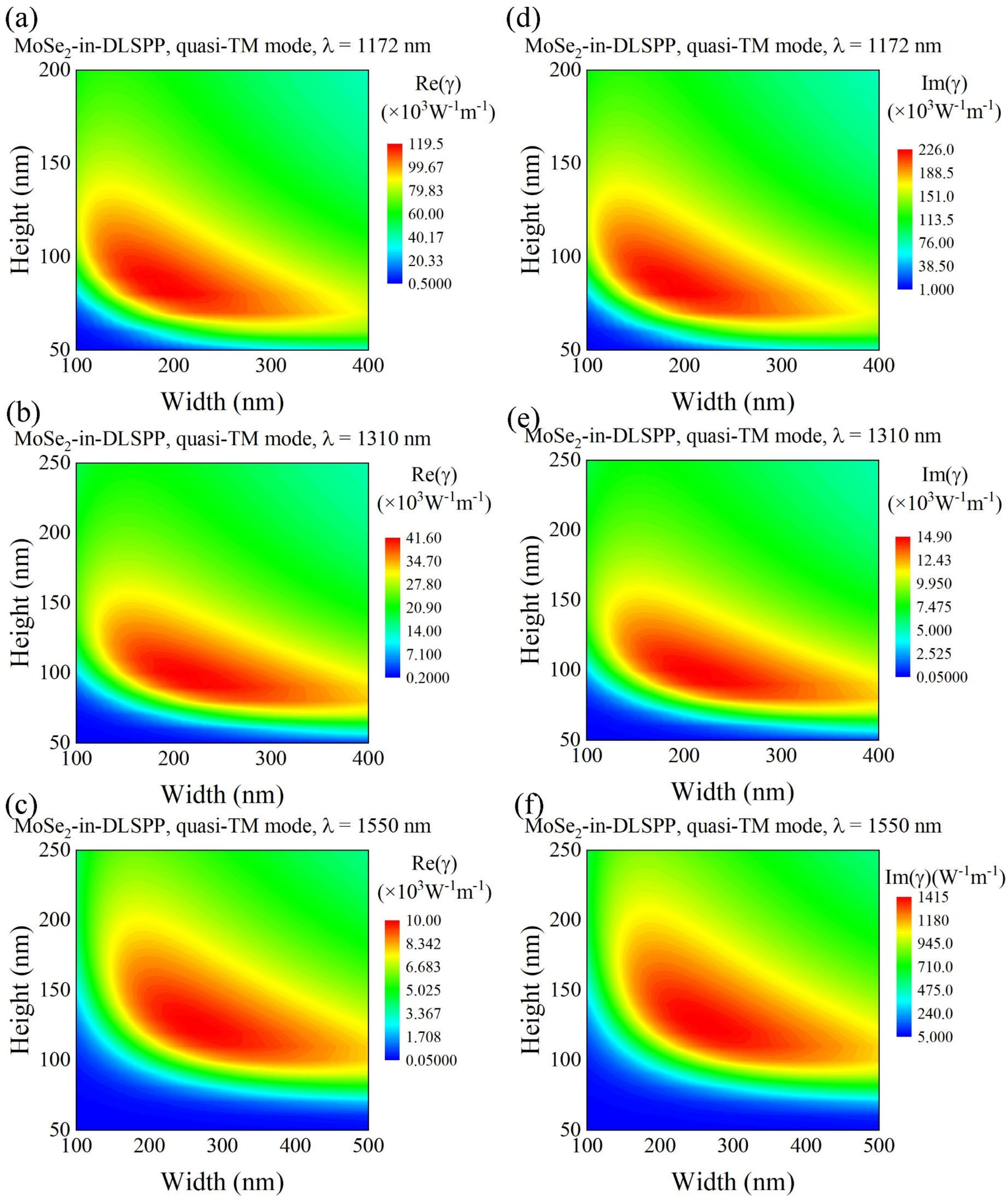

Fig. 5. Real part of nonlinear parameters of monolayer-$MoSe_2$-in-DLSPP waveguide in quasi-TM mode as a function of waveguide core width (x-axis) and height (y-axis) at (**a**) 1172 nm, (**b**) 1310 nm, (**c**) 1550 nm, and imaginary part of nonlinear parameters at (**d**) 1172 nm, (**e**) 1310 nm, and (**f**) 1550 nm. The insets show the waveguide cross sections when the maximum nonlinear parameter is taken at the respective wavelengths, respectively.

conduct a tolerance analysis on the monolayer-MoSe2-in-DLSPP waveguide optimized geometry, as shown in Table S2 (see the Supplementary Material). Simultaneously, we summarize and compare the maximum absolute values of Re(γ) and Im(γ) for the monolayer-MoS_2-, WS_2-, $MoSe_2$-, WSe_2-in-DLSPP waveguides at the three representative wavelengths, as shown in Fig. 6. Due to the eminent NLO characteristics of monolayer TMDCs, all the monolayer-TMDCs-in-DLSPP waveguides possess much greater absolute values of Re(γ) and Im(γ) than that of pure DLSPP waveguides. Furthermore, spectral dependence of the maximized absolute values of Re(γ) and Im(γ) for all the monolayer-TMDCs-in-DLSPP waveguides are quantitatively studied over a broad

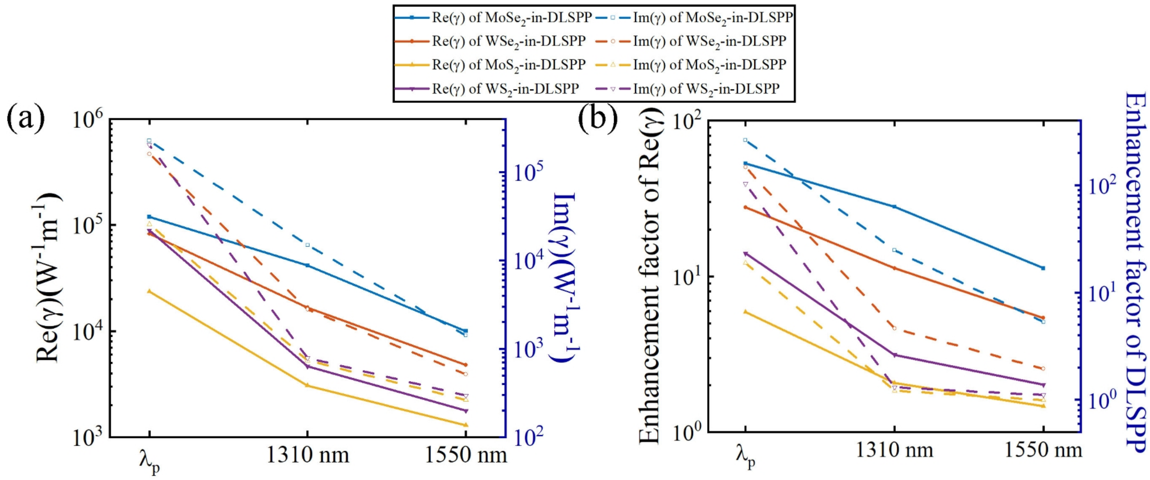

Fig. 6. (**a**) Maximum nonlinear parameters obtained at three different wavelengths (exciton resonance peak $\lambda_p = 1172$ nm, communication wavelength $\lambda = 1310$ nm, 1550 nm) in quasi-TE mode of the monolayer-$MoSe_2$-in-DLSPP waveguide, and (**b**) its comparison with nonlinear parameters of the pure DLSPP waveguide.

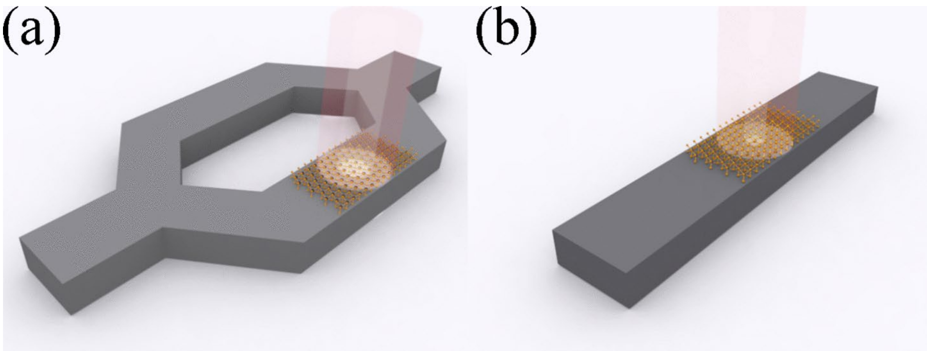

Fig. 7. Schematic of (**a**) MZI phase modulator, (**b**) extinction modulator based on the monolayer-TMDCs-on-SOI waveguide.

wavelength range from 1100 to 1550 nm, as illustrated in Figs. S7-S10 (see the Supplementary Material). Finally, the propagation losses of pure SOI and TMDCs-on-SOI waveguides, as well as DLSPP and TMDCs-in-DLSPP waveguides, are calculated, as shown in Table S3 (see the Supplementary Material).

Superb performance of all-optical modulators based on the waveguides

In this section, we utilize the above results to demonstrate the phase modulation and extinction modulation performance of waveguides integrated with monolayer-TMDCs. Despite the promising potential of monolayer-TMDCs-in-DLSPP waveguides with their giant nonlinear parameters, their practical application is hindered by significant linear losses caused by the metal layer. As a consequence, we exploit the monolayer-TMDCs-on-SOI with the optimized geometry to construct the all-optical nonlinear phase and extinction modulators, which is easier to interact with optical pump. As can be seen from Fig. 7a, in the nonlinear phase modulator, one arm of the Mach-Zehnder interferometer (MZI) is integrated with monolayer TMDCs to attain a π-phase shift, in order to achieve the constructive/destructive interference and the resultant maximized contrast between the on/off states. The reason why we only integrate one arm of MZI with monolayer TMDCs is to minimize the insertion loss[29]. Initially, the results of the coupling loss of MZI integrated with monolayer TMDCs indicate low loss value, demonstrating efficient light propagation within the modulator and confirming the feasibility of MZI, as shown in Fig. S11-S13 (see the Supplementary Material). Thus we can calculate its modulation efficiency, i.e., the phase modulation effect per unit length, as

$$\Delta\varphi = \frac{2\pi}{\lambda_0}\Delta n_{wg} \tag{4}$$

where $\Delta n_{wg} = n_{2\text{eff}} I$ is the variation of the waveguide phase coefficient, due to maximum and minimum applied local optical intensity, $n_{2\text{eff}}$ refers to the nonlinear refractive index of the waveguide and is another way to characterize the nonlinear refractive properties of a waveguide, I is the optical pump intensity. The maximum phase shift of the nonlinear phase modulator can be calculated by[30]:

$$\Delta\varphi_{max} = \frac{2\pi}{\lambda_0}\Delta n_{wg} \times L_{eff}\left(I\right) \tag{5}$$

where $L_{eff}\left(I\right) = \left(1 - \exp\left(-\alpha L\right)\right)/\alpha$ is effective length of the waveguide, α(I) refers to the damping factor of the waveguide.

The all-optical absorption modulator is an optical device used to achieve all-optical domain signal modulation and control without the need for an applied voltage. It utilizes the absorption and nonlinear optical effects of light in materials to realize modulation of optical signals, as shown in Fig. 7b. The optical loss per unit length can be written as

$$\Delta\alpha = \frac{4\pi}{\lambda_0}\Delta k_{wg} \tag{6}$$

where $\Delta k_{wg} = \lambda_0 \beta_{eff} I/4\pi$ is the variation of the waveguide extinction coefficient, due to maximum and minimum applied local optical intensity, β_{eff} denotes the β of the waveguide. The maximum extinction change of the nonlinear extinction modulator could be computed as

$$\Delta\alpha_{max} = \frac{4\pi}{\lambda_0}\Delta k_{wg} \times L_{eff}\left(I\right) \tag{7}$$

the optical pump intensity used in the following calculation will be much smaller than the saturation term of monolayer TMDCs 2PA[31,32], therefore we will ignore the saturation term of monolayer TMDCs 2PA below.

Taking monolayer-$MoSe_2$-on-SOI waveguides as examples, we characterize and optimize the performance of the corresponding all-optical nonlinear modulators at the three representative wavelengths. First of all, we investigate the properties of all-optical nonlinear phase modulators based on MZI. Fig. 8a demonstrates the modulation efficiency of a phase modulator based on monolayer-$MoSe_2$-on-SOI as a function of the optical pump intensity at three characteristic wavelengths, which can be calculated by Eq. 4. It can be observed that since monolayer $MoSe_2$ is a material without saturable absorption, the modulation efficiency increases with increasing optical power without any saturation effects. The modulator based on integrated silicon waveguides with monolayer $MoSe_2$ exhibits modulation efficiencies of 0.73 π/mm at the λ_p, 0.35 π/mm at 1310 nm, and 0.15 π/mm at 1550 nm under an optical pump intensity of 1 GW/cm^2. Figure 8b shows the L_{eff} required to achieve a π-phase modulation in an all-optical phase modulator under different optical pump intensities at three characteristic wavelengths. Based on a monolayer $MoSe_2$-integrated silicon waveguide all-optical phase modulator, the required L_{eff} to achieve π-phase modulation is 1.36 mm, 2.83 mm, and 6.79 mm at the λ_p, 1310 nm, and 1550 nm, respectively, when the optical pump intensity is 1 GW/cm^2. In addition to this, we summarize the modulation efficiency and effective modulation length of four monolayer-TMDCs-on-SOI waveguide modulators at an optical pump intensity of 1 GW/cm^2 in Tables S4 and S5 (see the Supplementary Material), respectively.

The extinction modulation efficiency of silicon waveguides integrated with monolayer TMDCs can be calculated using Eq. 6. Similar to all-optical phase modulators, the all-optical extinction modulation efficiency increases with increasing optical intensity, as shown in Fig. 8c. For a monolayer-$MoSe_2$-on-SOI waveguide all-optical extinction modulator, the modulation efficiencies under an optical pump intensity of 1 GW/cm^2 are 39.92 dB/mm, 3.45 dB/mm, and 0.51 dB/mm at λ_p, 1310 nm and 1550 nm, respectively. Figure 8d illustrates the required L_{eff} for achieving 3 dB extinction modulation in an all-optical phase modulator at three characteristic wavelengths as a function of the optical pump intensity. For an all-optical extinction modulator based on a monolayer-$MoSe_2$-on-SOI waveguide, the required L_{eff} to achieve 3 dB extinction modulation is 5.85 mm, 0.87 mm, and 75 μm at the λ_p, 1310 nm, and 1550 nm, respectively, under an optical pump intensity of 1 GW/cm^2. Furthermore, we present a summary of the modulation efffciency, effective modulation length and extinction ration of four monolayer-TMDCs-on-SOI waveguide modulators under an optical pump intensity of 1 GW/cm^2 in Tables S6, S7 and S8 (see the Supplementary Material), respectively.

A comparative performance evaluation was conducted for monolayer-$MoSe_2$-on-SOI waveguide devices against a typical nonlinear graphene-based waveguide. The graphene-on-silicon (GOS) waveguide phase modulator is required to achieve a π-phase modulation with a modulation length of 1.5 cm under an optical intensity of 0.3 GW/cm^2 [33]. Our designed phase modulator requires a modulation length nearly an order of magnitude smaller than the modulation length required for the GOS waveguide phase modulator under an optical intensity of 1 GW/cm^2. Furthermore, the GOS waveguide phase modulator requires 220 μm to achieve 3 dB extinction modulation under an optical intensity of 10 MW/cm^2. At the λ_p, the modulation length of our designed modulator is shorter than that required for GOS extinction modulators. Although the optical pump intensity required for our designed monolayer-$MoSe_2$-on-SOI waveguide is slightly higher, our designed waveguides circumvent the issue of linear loss observed in GOS waveguides. Additionally, we have summarized the information in Tables S8 and S9 (see the Supplementary Material). In summary, compared to graphene-based nonlinear modulators, our designed nonlinear modulator based on monolayer $MoSe_2$ exhibits excellent

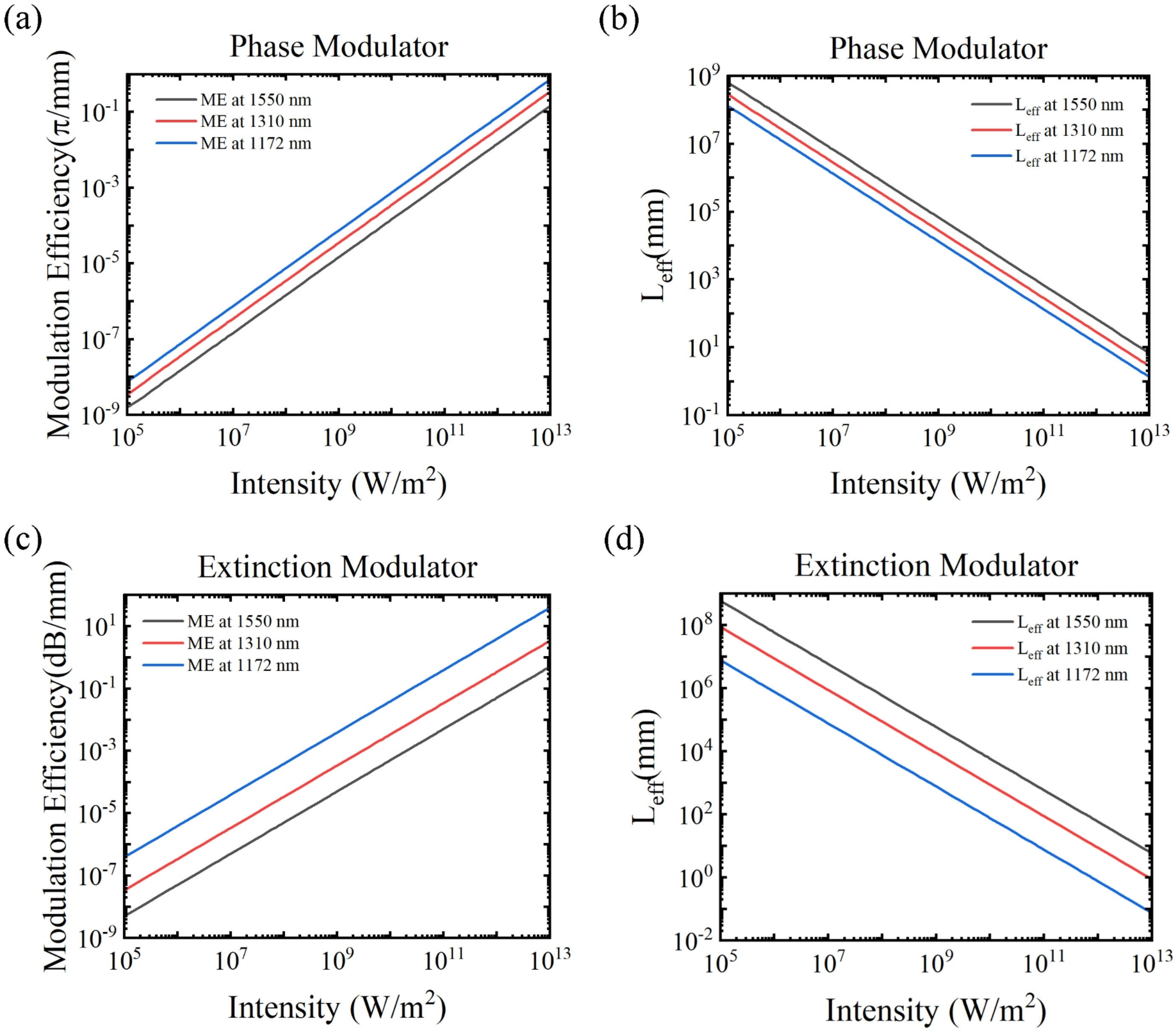

Fig. 8. (**a**) Modulation efficiency and (**b**) effective modulation length of monolayer-$MoSe_2$-on-SOI all-optical phase modulator as a function of optical pump intensity at three characteristic wavelengths. (**c**) Modulation efficiency and (**d**) effective modulation length of monolayer-$MoSe_2$-on-SOI all-optical extinction modulator as a function of optical pump intensity at three characteristic wavelengths.

performance in both phase modulation and extinction modulation. The increase in optical intensity allows for a further reduction in the length of the modulator, enhancing flexibility and adjustability in system design. This indicates that monolayer-TMDCs-on-SOI waveguides can achieve compact and efficient optical modulators, supporting applications in the optical communication and networking fields.

Conclusion

We investigated the influence of monolayer TMDCs on the nonlinear parameters of silicon photonic waveguides and gold-based DLSPP waveguides over a wide spectral range from the excitonic resonant peak (λ_p) to 1550 nm. Taking monolayer $MoSe_2$ as an example, after integrating it into SOI waveguides, we obtained a maximum $Re(\gamma)$ of 5001.87 $W^{-1}m^{-1}$ and a maximum imaginary part of 8910.76 $W^{-1}m^{-1}$ at the λ_p in the quasi-TE mode. These values exceed those of SOI waveguides without monolayer $MoSe_2$ by more than 7 times and 33 times, respectively. The nonlinear parameters in the quasi-TM mode are much lower than those in the quasi-TE mode, mainly due to the extremely low optical field intensity at the core-cladding boundary where monolayer $MoSe_2$ is located. For the monolayer-$MoSe_2$-in-DLSPP waveguide at the λ_p, optimized geometry yielded a real part of the nonlinear parameter of 119111.94 $^{-1}m^{-1}$ and an imaginary part of 225534.04 $^{-1}m^{-1}$, which are 53 times and 262 times larger, respectively, than those of DLSPP waveguides without monolayer $MoSe_2$.

Furthermore, based on the optimized two-dimensional TMDCs-silicon waveguide composite structure, we further investigated the all-optical modulation performance of the monolayer-$MoSe_2$-on-SOI waveguide. Based on a monolayer $MoSe_2$-integrated silicon waveguide all-optical phase modulator, the required L_{eff} to achieve π -phase modulation is 1.36 mm, 2.83 mm, and 6.79 mm at the λ_p, 1310 nm, and 1550 nm, respectively, when the optical pump intensity is 1 GW/cm^2. For an all-optical extinction modulator based on a monolayer-$MoSe_2$-on-SOI waveguide, the required L_{eff} to achieve 3 dB extinction modulation is 5.85 mm, 0.87 mm, and 75 μm at the λ

$_p$, 1310 nm, and 1550 nm, respectively, under an optical pump intensity of 1 GW/cm^2. Our designed waveguides circumvent the issue of linear loss observed in GOS waveguides. It is worth noting that with increasing optical intensity, the length of the modulator can be further reduced, providing greater flexibility and tunability for system design in practical applications. This implies that integrated waveguides based on monolayer TMDCs can achieve more compact and efficient optical modulators, providing strong support for applications in the optical communication and networks.

Methods
The interaction between light and TMDCs within the waveguide optical modes is characterized by the nonlinear parameter. The parameter was calculated using a two-dimensional full-vector finite element method (FEM) in COMSOL Multiphysics 6.0. Simulations were performed at free-space wavelengths of $\lambda = 1550$ nm, 1310 nm, and at the exciton resonance peaks of the TMDCs. In all COMSOL simulations, the monolayer thicknesses were set to 0.97 nm for $MoSe_2$, 0.76 nm for WSe_2, 0.71 nm for MoS_2, and 0.81 nm for WS_2. The waveguide substrate made of SOI was sized at 10 µm × 5 µm, with an air (or PMMA) cladding of the same dimensions. Additionally, an 800 nm perfectly matched layer (PML) was placed around the air (PMMA) cladding and SOI substrate to simulate an open boundary with no reflections. The mesh was controlled by the physics-controlled network, with the element size set to "Extremely fine."

Supplementary Information
The supplementary material contains ten supplementary figures, cited in the test as Figs. S1–S10, and four tables, cited as Tables S1–S4.

Data availability
The data that support the findings of this study are available from the corresponding author upon reasonable request.

Received: 18 June 2024; Accepted: 18 December 2024
Published online: 02 January 2025

References

1. Santos, I., Castro, L., Rodriguez-Fernandez, N., Torrente-Patiño, Á. & Carballal, A. *Artificial neural networks and deep learning in the visual arts: A review* https://doi.org/10.1007/s00521-020-05565-4 (2021).
2. Bristow, A. D., Rotenberg, N. & Van Driel, H. M. Two-photon absorption and Kerr coefficients of silicon for 850–2200 nm. [*Appl. Phys. Lett.* https://doi.org/10.1063/1.2737359 (2007).
3. Chhowalla, M., Liu, Z. & Zhang, H. Two-dimensional transition metal dichalcogenide (TMD) nanosheets. *Chem. Soc. Rev.* **44**, 2584–2586. https://doi.org/10.1039/c5cs90037a (2015).
4. Li, W. et al. Ultrafast all-optical graphene modulator. *Nano Lett.* **14**, 955–959. https://doi.org/10.1021/nl404356t (2014).
5. Yu, S. et al. All-optical graphene modulator based on optical kerr phase shift. *Optica* **3**, 541–544. https://doi.org/10.1364/OPTICA.3.000541 (2016).
6. He, X. et al. On-chip two-dimensional material-based waveguide-integrated photodetectors. *J. Mater. Chem. C* **12**, 2279–2316. https://doi.org/10.1039/D3TC03679K (2024).
7. Ooi, K. J. A., Ang, L. K. & Tan, D. T. H. Waveguide engineering of graphene's nonlinearity. *Appl. Phys. Lett.* **105**, 111110 (2014).
8. Flöry, N. et al. Waveguide-integrated van der waals heterostructure photodetector at telecom wavelengths with high speed and high responsivity. *Nat. Nanotechnol.* **15**, 118–124. https://doi.org/10.1038/s41565-019-0602-z (2020).
9. Lin, Y. et al. Monolithically integrated, broadband, high-efficiency silicon nitride-on-silicon waveguide photodetectors in a visible-light integrated photonics platform. *Nat. Commun.* **13**, 6362. https://doi.org/10.1038/s41467-022-34100-3 (2022).
10. Wang, Q. H., Kalantar-Zadeh, K., Kis, A., Coleman, J. N. & Strano, M. S. Electronics and optoelectronics of two-dimensional transition metal dichalcogenides. *Nat. Nanotechnol.* **7**, 699–712. https://doi.org/10.1038/nnano.2012.193 (2012).
11. Koppens, F. H. L. et al. Photodetectors based on graphene, other two-dimensional materials and hybrid systems. *Nat. Nanotechnol.* **9**, 780–793. https://doi.org/10.1038/nnano.2014.215 (2014).
12. Weng, B., Zhang, X., Zhang, N., Tang, Z. R. & Xu, Y. J. Two-dimensional MoS^2 nanosheet-coated $\mathrm{Bi_2S_3}$ Discoids: Synthesis, formation mechanism, and photocatalytic application. *Langmuir* **31**, 4314–4322. https://doi.org/10.1021/la504549y (2015).
13. Koo, J. et al. Near-infrared saturable absorption of defective bulk-structured $\mathrm{WTe_2}$ for femtosecond laser mode-Locking. *Adv. Funct. Mater.* **26**, 7454–7461. https://doi.org/10.1002/adfm.201602664 (2016).
14. Mueller, T. & Malic, E. Exciton physics and device application of two-dimensional transition metal dichalcogenide semiconductors. *npj 2D Mater. Appl.* **2**, 29, https://doi.org/10.1038/s41699-018-0074-2 (2018).
15. Zhou, F., Kua, J. H., Lu, S. & Ji, W. Two-photon absorption arises from two-dimensional excitons. *Opt. Exp.* **26**, 16093. https://doi.org/10.1364/oe.26.016093 (2018).
16. Zhou, F. & Ji, W. Two-photon absorption and subband photodetection in monolayer MoS^2. *Opt. Lett.* **42**, 3113. https://doi.org/10.1364/ol.42.003113 (2017).
17. Cunningham, G. et al. Solvent exfoliation of transition metal dichalcogenides: Dispersibility of exfoliated nanosheets varies only weakly between compounds. *ACS Nano* **6**, 3468–3480. https://doi.org/10.1021/nn300503e (2012).
18. Liu, H. L. et al. Optical properties of monolayer transition metal dichalcogenides probed by spectroscopic ellipsometry. *Appl. Phys. Lett.*[SPACE]https://doi.org/10.1063/1.4901836 (2014).
19. Yim, C. et al. Investigation of the optical properties of MoS^2 thin films using spectroscopic ellipsometry. *Appl. Phys. Lett.* **104**, 103114. https://doi.org/10.1063/1.4868108 (2014).
20. Eichfeld, S. M., Eichfeld, C. M., Lin, Y.-C., Hossain, L. & Robinson, J. A. Rapid, non-destructive evaluation of ultrathin $\mathrm{WSe_2}$ using spectroscopic ellipsometry. *APL Mater.*[SPACE]https://doi.org/10.1063/1.4893961 (2014).
21. Park, H. G. et al. Temperature dependence of the critical points of monolayer MoS^2 by ellipsometry. *Appl. Spectro. Rev.* **51**, 621–635. https://doi.org/10.1080/05704928.2016.1166436 (2016).
22. Qiu, D. Y., da Jornada, F. H. & Louie, S. G. Optical spectrum of MoS^2: Many-body effects and diversity of exciton states. *Phys. Rev. Lett.* **111**, 216805. https://doi.org/10.1103/PhysRevLett.111.216805 (2013).
23. Molina-Sánchez, A., Sangalli, D., Hummer, K., Marini, A. & Wirtz, L. Effect of spin-orbit interaction on the optical spectra of single-layer, double-layer, and bulk MoS^2. *Phys. Rev. B* **88**, 045412. https://doi.org/10.1103/PhysRevB.88.045412 (2013).

24. Liu, H. L. et al. Temperature-dependent optical constants of monolayer MoS^2, MoSe_2, WS_2, and WSe_2: spectroscopic ellipsometry and first-principles calculations. *Sci. Rep.* **10**, 15282. https://doi.org/10.1038/s41598-020-71808-y (2020).
25. Zhou, F., Nieva, C. J., Fan, D., Lu, S. & Ji, W. Superior optical Kerr effects induced by two-dimensional excitons. *Photon. Res.* **10**, 834. https://doi.org/10.1364/prj.447029 (2022).
26. Zhang, X., Qiu, J., Li, X., Zhao, J. & Liu, L. Complex refractive indices measurements of polymers in visible and near-infrared bands. *Appl. Opt.* **59**, 2337. https://doi.org/10.1364/ao.383831 (2020).
27. Schinke, C. et al. Uncertainty analysis for the coefficient of band-to-band absorption of crystalline silicon. *AIP Adv.*[SPACE]https://doi.org/10.1063/1.4923379 (2015).
28. Malitson, I. H. Interspecimen comparison of the refractive index of fused silica*,†. *J. Opt. Soc. Am.* **55**, 1205. https://doi.org/10.1364/josa.55.001205 (1965).
29. Ji, Y. et al. An electronic Mach-Zehnder interferometer. *Nature* **422**, 415–418. https://doi.org/10.1038/nature01503 (2003).
30. Ojaghi, S., Golmohammadi, S. & Soofi, H. All-optical graphene-on-silicon slot waveguide modulator based on graphene's Kerr effect. *Appl. Opt.* **60**, 7945. https://doi.org/10.1364/ao.427755 (2021).
31. Dong, N. et al. Saturation of two-photon absorption in layered transition metal dichalcogenides: Experiment and theory. *ACS Photon.* **5**, 1558–1565. https://doi.org/10.1021/acsphotonics.8b00010 (2018).
32. Zhang, S. et al. Direct observation of degenerate two-photon absorption and its saturation in WS_2 and MoS^2 monolayer and few-layer films. *ACS Nano* **9**, 7142–7150. https://doi.org/10.1021/acsnano.5b03480 (2015).
33. Ooi, K. J. A., Leong, P. C., Ang, L. K. & Tan, D. T. H. All-optical control on a graphene-on-silicon waveguide modulator. *Sci. Rep.* **7**, 12748. https://doi.org/10.1038/s41598-017-13213-6 (2017).

Author contributions
Tianyang Ding conducted simulations and wrote the manuscript. All authors reviewed the manuscript.

Declarations

Competing interests
The authors declare no competing interests.

Additional information
Supplementary Information The online version contains supplementary material available at https://doi.org/10.1038/s41598-024-83898-z.

Correspondence and requests for materials should be addressed to T.D.